Polar stratospheric nitric acid depletion surveyed from a decadal dataset of IASI total columns

Gaetane Ronsmans[1], Catherine Wespes[1,*], Lieven Clarisse[1], Susan Solomon[2], Daniel Hurtmans[1], Cathy Clerbaux[1,3], and Pierre-François Coheur[1]

[1]Université libre de Bruxelles (ULB), Spectroscopy, Quantum Chemistry and Atmospheric Remote Sensing (SQUARES), Brussels, Belgium
[2]Department of Earth, Atmospheric and Planetary Sciences, Massachusetts Institute of Technology, Cambridge, Massachusetts, USA
[3]LATMOS/IPSL, Sorbonne Université, UVSQ, CNRS, Paris, France

Correspondence: Catherine Wespes (cwespes@ulb.ac.be)

Abstract

In this paper, we exploit the first 10-year data-record (2008-2017) of nitric acid (HNO_3) total columns measured by the IASI-A/Metop infrared sounder, characterized by an exceptional daily sampling and a good vertical sensitivity in the mid-stratosphere (around 50 hPa), to monitor the causal relationship between the temperature decrease and the observed HNO_3 loss that occurs each year in the Antarctic stratosphere during the polar night. Since the HNO_3 depletion results from the formation of polar stratospheric clouds (PSCs) which trigger the development of the ozone (O_3) hole, its continuous monitoring is of high importance. We verify here, from the 10-year time evolution of the pair $HNO3$-temperature (taken from reanalysis at 50 hPa), the recurrence of specific regimes in the cycle of IASI HNO_3 and identify, for each year, the day and the 50 hPa temperature ("drop temperature") corresponding to the onset of strong HNO_3 depletion in the Antarctic winter. Although the measured HNO_3 total column does not allow differentiating the uptake of HNO_3 by different types of PSC particles along the vertical profile, an average drop temperature of ~194.2 ± 3.8 K, ~~consistent with~~ close to the nitric acid trihydrate (NAT) ~~formation temperature~~ existence threshold (~~close to~~ ~195 K at 50 hPa), is found in the region of potential vorticity lower than -10×10⁻⁵ $K.m^2.kg^{-1}.s^{-1}$ (similar to the 70° – 90° S Eqlat region during winter). The spatial distribution and inter-annual variability of the drop temperature are investigated and discussed ~~in the context of previous PSCs studies~~. This paper highlights the capability of the IASI sounder to monitor the long-term evolution of the polar stratospheric composition and processes involved in the depletion of stratospheric O_3.

1 Introduction

The cold and isolated air masses found within the polar vortex during winter are associated with a strong denitrification of the stratosphere due to the formation of PSCs (composed of HNO_3, sulphuric acid (H_2SO_4) and water ice (H_2O)) (Peter, 1997; Voigt et al., 2000; von König, 2002; Schreiner et al., 2003; Peter and Grooß, 2012). These clouds strongly affect the polar chemistry by (1) acting as surfaces for the heterogeneous activation of chlorine and bromine compounds, in turn leading to enhanced O3 destruction (Solomon, 1999; Wang and Michelangeli, 2006; Harris et al., 2010; Wegner et al., 2012) and by (2) removing gas-phase HNO_3 temporarily or permanently through uptake by PSCs and sedimentation of large PSC particles to lower altitudes. The denitrification of the polar stratosphere during winter delays the reformation of chlorine reservoirs and, hence, intensifies the O_3 hole (Solomon, 1999; Harris et al., 2010). The heterogeneous reaction rates on PSCs surface and the uptake of HNO_3 strongly depend on the temperature and on the PSCs particle type. The PSCs are classified into three

3different types based on their composition and optical properties: type Ia solid nitric acid trihydrate - NAT ($HNO_3.(H_2O)_3$), type Ib liquid supercooled ternary solution - STS ($HNO_3/H_2SO_4/H_2O$ with variable composition) and type II, crystalline water-ice particles (likely composed of a combination of different chemical phases) (Toon et al., 1986; Koop et al., 2000; Voigt et al., 2000; Lowe and MacKenzie, 2008). In the stratosphere, they mostly consist of mixtures of liquid/solid STS/NAT particles in varying number densities, with HNO_3 being the major constituent of these particles. The large-size NAT particles of low number density are the principal cause of sedimentation (Lambert et al., 2012; Pitts et al., 2013; Molleker et al., 2014; Lambert et al., 2016). The formation temperature of STS (T_{STS}) and the thermodynamic equilibrium temperatures of NAT (T_{NAT}) and ice (T_{ice}), have been determined, respectively, as: ~192 K (Carslaw et al., 1995), ~195.7 K (Hanson and Mauersberger, 1988) and ~188 K (Murphy and Koop, 2005) for typical 50 hPa atmospheric conditions (5 ppmv H_2O and 10 ppbv HNO_3). While the NAT nucleation was thought to require temperatures below T_{ice} and pre-existing ice particles, recent observational and modelling studies have shown that HNO_3 starts to condense in early PSC season in liquid NAT mixtures well above T_{ice} (~4 K below T_{NAT} , close to T_{STS}) even after a very short temperature threshold exposure (TTE) to these temperatures but also slightly below T_{NAT} after a long TTE, whereas the NAT existence persists up to T_{NAT} (Pitts et al., 2013; Hoyle et al., 2013; Lambert et al., 2016; Pitts et al., 2018). It has been recently proposed that the higher temperature condensation results from heterogeneous nucleation of NAT on meteoritic dust in liquid aerosol (Hoyle et al., 2013; Grooß et al., 2014; James et al., 2018). Further cooling below T_{STS} and T_{ice} leads to nucleation of liquid STS, of solid NAT onto ice and of ice particles mainly from STS (type II PSCs) (Lowe and MacKenzie, 2008). The formation of NAT and ice has also been shown to be triggered by stratospheric mountain-waves (Carslaw et al., 1998; Hoffmann et al., 2017). Although the formation mechanisms and composition of STS droplets in stratospheric conditions are well described (Toon et al., 1986; Carslaw et al., 1995; Lowe and MacKenzie, 2008), the NAT and ice nucleation processes still require further investigation. This could be important as the chemistry-climate models (CCMs) generally oversimplify the heterogeneous nucleation schemes for the PSCs formation (Zhu et al., 2015; Spang et al., 2018; Snels et al., 2019) preventing an accurate estimation of O_3 levels. The influence of HNO_3 in modulating O_3 abundances in the stratosphere is furthermore underrepresented in CCMs (Kvissel et al., 2012).

Several satellite instruments measure stratospheric HNO_3 (e.g. MLS/UARS (Santee et al., 1999), MLS/Aura (Santee et al., 2007), MIPAS/ENVISAT (Piccolo and Dudhia, 2007), ACE-FTS/SCISAT (Sheese et al., 2017) and SMR/Odin (Urban et al., 2009)). The spaceborne lidars CALIOP/CALIPSO and the infrared instrument MIPAS/Envisat) are capable to detect and classify the PSC types, and to follow their formation mechanisms (Lambert et al., 2016; Pitts et al., 2018; Spang et al., 2018) and references therein, which complements in situ measurements (Voigt et al., 2005) and ground-based lidar (Snels et al., 2019). From these available observational datasets, the HNO_3 depletion has been linked to the PSCs formation and detected below the T_{NAT} threshold (Santee et al., 1999; Urban 55 et al., 2009; Lambert et al., 2016; Ronsmans et al., 2018), but its relationship to PSCs still needs further investigation given the complexity of the nucleation mechanisms that depends on a series of parameters (e.g. atmospheric temperature, water and HNO_3 vapour pressure, time exposure to temperatures, temperature history).

In contrast to the limb satellite instruments mentioned above, the infrared nadir sounder IASI offers a dense spatial sampling of the entire globe, twice a day (Section 2). While it cannot provide a vertical profile of HNO_3 similar to the limb sounders, IASI provides reliable total column measurements of HNO_3 characterized by a maximum sensitivity in the low-middle stratosphere around 50 hPa (20 km) during the dark Antarctic winter (Ronsmans et al., 2016, 2018) where the PSCs cloud form (Voigt et al., 2005; Lambert et al., 2012; Spang et al., 2016, 2018). This study aims to explore the 10-years continuous HNO_3 measurements from IASI for providing a long-term global picture of depletion and of its

98   dependence to temperatures during polar winter (Section 3). The temperature corresponding to the onset
99   of the strong depletion in HNO₃ records (here referred to as 'drop temperature') is identified in Section
100 4 for each observed year and discussed in the context of previous studies.
101
102 **2 Data**
103
104 The HNO₃ data used in the present study are obtained from measurements of the Infrared Atmospheric
105 Sounding Interferometer (IASI) embarked on the Metop-A satellite. IASI measures the Earth's and
106 atmosphere's radiation in the thermal infrared spectral range (645 - 2760 cm^{-1}), with a 0.5 cm^{-1} apodized
107 resolution and a low radiometric noise (Clerbaux et al., 2009; Hilton et al., 2012). Thanks to its polar
108 sun-synchronous orbit with more than 14 orbits a day and a field of view of four simultaneous footprints
109 of 12 km at nadir, IASI provides global coverage twice a day (9.30 AM and PM mean local solar time).
110 That extensive spatial and temporal sampling in the polar regions is key to this study.
111
112 The HNO₃ vertical profiles are retrieved on a uniform vertical 1 km grid of 41 layers (from the surface
113 to 40 km with an extra layer above to 60 km) in near-real-time by the Fast Optimal Retrieval on Layers
114 for IASI (FORLI) software, using the optimal estimation method (Rodgers, 2000). Detailed information
115 on the FORLI algorithm and retrieval parameters specific to HNO₃ can be found in previous papers
116 (Hurtmans et al., 2012; Ronsmans et al., 2016). For this study, only the total columns (v20151001) are
117 used, considering (1) the low vertical resolution of IASI with only one independent piece of information
118 (FWHM of the averaging kernels of ~30 km), (2) the limited sensitivity of IASI to tropospheric HNO₃,
119 (3) the dominant contribution of the stratosphere to the HNO₃ total column and (4) the largest sensitivity
120 of IASI in the region of interest, i.e. in the low and mid-stratosphere (from ~70 to ~30 hPa), where the
121 HNO₃ abundance is the highest (Ronsmans et al., 2016). The IASI measurements capture the expected
122 variations of HNO₃ within the polar night, as illustrated in Fig. 1 that shows examples of vertical HNO₃
123 profiles retrieved within the dark Antarctic vortex (above Arrival Height) and outside the vortex (above
124 Lauder). The retrieved profiles are shown along with their associated total retrieval error and averaging
125 kernels (the total column averaging kernels and the so-called "sensitivity profile" are also represented;
126 see Ronsmans et al., 2016 for more details). Above Arrival Height during the dark Antarctic winter, we
127 clearly see depleted HNO₃ levels in the low and mid-stratosphere and the altitude of maximum
128 sensitivity (at around 30 hPa for this case). At Lauder on the contrary, HNO₃ levels larger than the a
129 priori are observed in the stratosphere with a larger range of maximum sensitivity. The total columns are
130 associated with a total retrieval error ranging from around 3% at mid- and polar latitudes to 25% above
131 cold Antarctic surface during winter (due to a weaker sensitivity above very cold surface with a DOFS
132 of 0.95 and to ~~an~~ poor knowledge of the seasonally and wavenumber-dependent emissivity above ice
133 surfaces which induces larger forward model errors), and a low bias (lower than 12%) in polar regions
134 over the altitude range where the IASI sensitivity is the largest, when compared to ground-based FTIR
135 measurements (see Hurtmans et al., 2012 and Ronsmans et al., 2016 for more details). In order to expand
136 on the comparisons against FTIR measurements which is not possible during the polar night, Fig. 2 (top
137 panel) presents the time series of daily IASI total HNO₃ columns co-located with MLS measurements
138 within 2.5x2.5 grid boxes, averaged in the 70°S–90°S equivalent latitude band. In order to account for
139 the vertical sensitivity of IASI, the averaging kernels associated with each co-located IASI retrieved
140 profiles were considered for this cross-comparison. The MLS profiles were first interpolated to the
141 FORLI pressure grids, then converted into column profiles. They were also extended down to the surface
142 by considering the FORLI-HNO3 a priori profile. Similar variations in the HNO₃ column are captured
143 by the two instruments, with an excellent agreement in particular for the timing of the strong HNO₃
144 depletion within the inner vortex core. Note that a similar good agreement between the two satellite
145 datasets is obtained in other latitude bands (see Fig. 2 bottom panel for the 50°S–70°S equivalent latitude
146 band; the other bands are not shown).~~In order to expand on the comparisons against FTIR measurements~~

Quality flags similar to those developed for O_3 in previous IASI studies (Wespes et al., 2017) were applied a posteriori to exclude data (i) with a corresponding poor spectral fit (e.g. based on quality flags rejecting biased or sloped residuals, fits with maximum number of iteration exceeded), (ii) with less reliability (e.g. based on quality flags rejecting suspect averaging kernels, data with less sensitivity characterized by a DOFS lower than 0.9) or (iii) with tropospheric cloud contamination (defined by a fractional cloud cover $\geq$ 25 %). Note that the HNO_3 total column distributions illustrated in sections below use the median as a statistical average since it is more robust against the outliers than the mean.

Temperature and potential vorticity (PV) fields are taken from the ECMWF ERA Interim Reanalysis dataset, respectively at 50 hPa and at the potential temperature of 530 K (corresponding to ~20 km altitude where the IASI sensitivity to HNO_3 is the highest during the Southern Hemisphere (S.H.) winter (Ronsmans et al., 2016). Because the HNO_3 uptake by PSCs starts a few degrees or slightly below T_{NAT} (~195.7 K at 50 hPa (Hanson and Mauersberger, 1988)) depending on the meteorological conditions (Pitts et al., 2013; Hoyle et al., 2013; Lambert et al., 2016; Pitts et al., 2018), a threshold temperature of 195 K is considered in the sections below to identify the PSCs-containing regions. The potential vorticity is used to delimit dynamically consistent areas in the polar regions. In what follows, we use either the equivalent latitudes ("eqlat", calculated from PV fields at 530 K) or the PV values to characterize the relationship between HNO_3 and temperatures in the cold polar regions. Uncertainties in ERA-Interim temperatures will also be discussed below.

3 Annual cycle of HNO₃ vs temperatures

Figure 2a shows the yearly HNO_3 cycle (solid lines, left axis) in the southernmost equivalent latitudes (70° - 90° S), as measured by IASI over the whole period of measurements (2008–2017). The total HNO_3 variability in such equivalent latitudes has already been discussed in a previous IASI study (Ronsmans et al., 2018) where the contribution of the PSCs into the HNO_3 variations was highlighted. The temperature time series, taken at 50 hPa, is here represented as well (dashed lines, right axis). From this figure, different regimes of HNO_3 total columns *vs* temperature can be observed throughout the year and from one year to another. In particular, we define here three main regimes (R1, R2 and R3) along the HNO_3/temperature cycle. The full cycle and the main regimes in the 70° - 90° S eqlat region are further represented in Fig. 2b that shows a histogram of the HNO_3 total columns as a function of temperature for the year 2011. Similar histograms are observed for the ten years of IASI measurements (not shown). The red horizontal and vertical lines in Fig. 2a and Fig. 2b, respectively, represent the 195 K threshold temperature used to identify the onset of HNO_3 uptake by PSCs (see Section 2). The three identified regimes correspond to:

- R1 is defined by the maxima in the total HNO_3 abundances covering the months of April and May (~3×10^{16} molec.cm^{-2}, R1 in Figures 2a and b), when the 50 hPa temperature strongly decreases (from ~220 to ~195 K). These high HNO_3 levels result from low sunlight, preventing photodissociation, along with the heterogeneous hydrolysis of N_2O_5 to HNO_3 during autumn before the formation of polar stratospheric clouds (Keys et al., 1993; Santee et al., 1999; Urban

196 et al., 2009; de Zafra and Smyshlyaev, 2001). This period also corresponds to the onset of the
197 deployment of the southern polar vortex which is characterized by strong diabatic descent with
198 weak latitudinal mixing across its boundary, isolating polar HNO_3-rich air from lower latitudinal
199 airmasses.
200
201 - R2 which extends from June to October is characterized by the onset of the strong decrease in
202 HNO_3 total columns at the beginning of June, when the temperatures fall below 195 K, followed
203 by a plateau of total HNO_3 minima. In this regime, the HNO_3 total columns average below 2×10^{16}
204 molec.cm^{-2} and the 50 hPa temperatures range mostly between 180 and 190 K.
205
206 - R3 starts in October when sunlight returns and the 50 hPa temperatures rise above 195 K. Despite
207 the stratospheric warming with 50 hPa temperatures up to 240 K in summer, the HNO_3 total
208 columns stagnate at the R2 plateau levels (around 1.5×10^{16} molec.cm^{-2}). This regime likely
209 reflects the photolysis of NO_3 and HNO_3 itself (Ronsmans et al., 2018) as well as the permanent
210 denitrification of the mid-stratosphere, caused by the PSCs sedimentation. The likely
211 renitrification of the lowermost stratosphere (Braun et al., 2019; Lambert et al., 2012) where the
212 HNO_3 concentrations and the IASI sensitivity to HNO_3 are lower (Ronsmans et al., 2016) can
213 hardly not be inferred from the IASI total column measurements. The plateau lasts until
214 approximately February, where HNO_3 total column slowly starts increasing, reaching the April-
215 May maximum in R1.
216
217 As illustrated in Fig. 32a, the three regimes are observed each year with, however, some interannual
218 variations. For instance, the sudden stratospheric warming (SSW) that occurs in 2010 (see the
219 temperature time series at 20 hPa for the year 2010; green dotted line) yielded higher HNO_3 total columns
220 (see green solid line in July and August) (de Laat and van Weele, 2011; Klekociuk et al., 2011; WMO,
221 2014; Ronsmans et al., 2018).
222
223 Figure 32c shows the evolution of the relationship between the daily averaged HNO_3 (calculated from a
224 7-day moving average) with the highest occurrence (in bins of 0.1×10^{16} molec.cm^{-2} and of 2K) and the
225 50 hPa temperature, over the 10 years of IASI. The red vertical line represents the 195 K threshold
226 temperature. Figure 32c clearly illustrates the slow increase in HNO_3 columns as the temperatures
227 decrease (February to May, i.e. R3 to R1), the strong and rapid HNO_3 depletion occurring in June (R2),
228 the plateau of low HNO_3 abundances in winter and spring (from August to November; R2 to R3). Figure
229 32c also highlights the interannual variability in total HNO_3, which is found to be the largest in R3, and
230 shows a strong consistency in the onset of the depletion between each year (beginning of June when the
231 temperatures fall below 195 K as indicated by the red vertical line). Given the span of PSCs formation
232 over a large range of altitudes (typically between 10 and 30 km) (Höpfner et al., 150 2006, 2009; Spang
233 et al., 2018; Pitts et al., 2018) and that of maximum IASI sensitivity to HNO_3 around 50 hPa (Hurtmans
234 et al., 2012; Ronsmans et al., 2016), the temperatures at two other pressure levels, namely 70 and 30 hPa
235 (i.e. ~15 and ~25 km), have also been tested to investigate the relationship between HNO_3 and
236 temperature in the low and mid-stratosphere. The results (not shown here) exhibit a similar HNO_3-
237 temperature behavior at the different levels with, as expected, lower and larger temperatures in R2,
238 respectively, at 30 hPa (down to ~180 K) and at 70 hPa (down to ~185 K), but still below the NAT
239 formation threshold at these pressure levels (T_{NAT} ~193 K at 30 hPa and ~197 K at 70 hPa) (Lambert et
240 al., 2016). Therefore, the altitude range of maximum IASI sensitivity to HNO_3 (see Section 2) is
241 characterized by temperatures that are below the NAT formation threshold at these pressure levels,
242 enabling the PSCs formation and the denitrification process. Furthermore, the consistency between the
243 195 K threshold temperature taken at 50 hPa and the onset of the strong total HNO_3 depletion seen in
244 IASI data (see Fig. 32a and Fig. 32c) is in agreement with the largest NAT area that starts to develop in

245 June around 20 km (Spang et al., 2018), which justifies the use of the 195 K temperature at that single
246 representative level in this study.
247
4 Onset of HNO₃ depletion and drop temperature detection

249
250 To identify the spatial and temporal variability of the onset of the depletion phase, the daily time
251 evolution of HNO_3 during the first 10 years of IASI measurements and the temperatures at 50 hPa are
252 explored. In particular, the second derivative of HNO_3 total column with respect to time is calculated to
253 detect the strongest rate of decrease seen in the HNO_3 time series and to identify its associated day and
254 50 hPa temperature.
255
4.1 HNO₃ vs temperature time series

257
258 Figure 3̶4 shows the time series of the second derivative of HNO_3 total column with respect to time
259 (blue) and of the temperature (red) averaged in the areas of potential vorticity smaller than -10×10⁻⁵
260 $K.m^2.kg^{-1}.s^{-1}$ to encompass the regions inside the inner polar vortex where the temperatures are the
261 coldest and the total HNO_3 depletion occurs (Ronsmans et al., 2018). The use of that PV threshold value
262 explains the gaps in the time series during the summer when the PV does not reach such low levels,
263 while the time series averaged in the 70°- 90° S Eqlat band (dashed blue for the second derivative of
264 HNO_3 and grey for the temperature) covers the full year. Note that the HNO_3 time series has been
265 smoothed with a simple spline data interpolation function to avoid gaps in order to calculate the second
266 derivative of HNO_3 total column with respect to time as the daily second-difference HNO_3 total column.
267 The horizontal red line shows the 195 K threshold.
268
269 As already illustrated in Fig. 3̶2a and Fig. 3̶2c, the strongest rate of HNO_3 depletion (i.e. the second
270 derivative minimum) is found around the 195 K threshold temperature, within some days (4 to 23 days)
271 after total HNO_3 reaches its maximum, i.e. typically between the 11th of May (2013) and the 8th of June
272 (2009). Except for the year 2014, T̶the 50 hPa drop temperatures are detected between 189.2 K and 198.6
273 K (194.1 K ± 2.8 K - 1σ standard deviation - on average over the 10 years, excluding 2014 that stands
274 out with a drop temperature of 202.8 K) 202.8 K, with an average of 194.2 ± 3.8 K (1σ standard
275 deviation) over the ten years. Knowing that T_{NAT} can be higher or lower depending on the atmospheric
276 conditions and that NAT starts to nucleate from ~2–4 K below T_{NAT} (Pitts et al., 2011; Hoyle et al., 2013;
277 Lambert et al., 2016), the results here tend to demonstrate the consistency between the 50 hPa drop
278 temperature, i.e. the temperature associated with the strongest HNO_3 depletion detected from IASI, and
279 the PSCs NAT formation temperature in th̶a̶te altitude region̶m̶i̶d̶-̶s̶t̶r̶a̶t̶o̶s̶p̶h̶e̶r̶e̶ ̶a̶t̶ ̶p̶o̶l̶a̶r̶ ̶l̶a̶t̶i̶t̶u̶d̶e̶s̶. Note
280 that the range observed in the 50 hPa drop temperature could reflect the preponderance by one type of
281 PSCs over another from one year to the next. The results̶I̶t̶ further justif̶yies the use of the single 50 hPa
282 level for characterizing and investigating the onset of HNO_3 depletion from IASI. Nevertheless, given
283 the range of maximum IASI sensitivity to HNO_3 around 50 hPa, typically between 70 and 30 hPa
284 (Ronsmans et al., 2016), the drop temperatures are also calculated at these two other pressure levels (not
285 shown here) to estimate the uncertainty of the calculated drop temperature defined in this study at 50
286 hPa. The 30 hPa and 70 hPa drop temperatures range respectively over 185.7 K –194.9 K and over 194.8
287 K – 203.7 K, with an average of 192.0 ± 2.9 K and 198.0 ± 3.2 K (1σ standard deviation) over the ten
288 years of IASI. The average values at 30 hPa and 70 hPa fall within the 1σ standard deviation associated
289 with the average drop temperature at 50 hPa. It is also worth noting the agreement between the drop
290 temperatures and the NAT formation threshold at these two pressure levels (T_{NAT} ~ 193 K at 30 hPa and
291 ~197 K at 70 hPa) (Lambert et al., 2016).
292

293 Figures 54a and b show the zonal distribution of HNO$_3$ total columns and of the temperature at 50 hPa,
294 respectively, spanning 55° - 90° S over the whole IASI period, with, superimposed, three isocontour
295 levels of potential vorticity (-10, -8 and -5×10^{-5} K.m^2.kg^{-1}.s^{-1} in blue, cyan and black, respectively) and
296 one isocontour for the 50 hPa temperature. The PV isocontour of -10×10^{-5} K.m^2.kg^{-1}.s^{-1} is clearly shown
297 to separate well the region of strong depletion in total HNO$_3$ according to the latitude and the time. The
298 red vertical dashed lines indicates the average date for the drop temperatures calculated in the area of PV$\leq$ -
299 10×10^{-5} K.m^2.kg^{-1}.s^{-1} (194.2 ± 3.8 K; see Fig. 43) over the IASI period. It shows that the strongest rate
300 in HNO$_3$ depletion occurs on average a few days before June. The delay of some days between the
301 maximum in total HNO$_3$ and the start of the depletion (see Fig. 43) is also visible in Fig. 54a. The yearly
302 zonally averaged time series over the ten years of IASI can be found in Fig. 65; it shows the
303 reproducibility of the edge of the collar HNO$_3$ region and of the region of the strong HNO$_3$ depletion,
304 respectively delimited by the PV isocontours of -5×10^{-5} K.m^2.kg^{-1}.s^{-1} and of -10×10^{-5} K.m^2.kg^{-1}.s^{-1} at 50
305 hPa, measured by IASI from year to year.
306
307 **4.2 Distribution of drop temperatures**
308
309 To explore the capability of IASI to monitor the onset of HNO$_3$ depletion at a large scale from year to
310 year, figure 76 shows the spatial distribution of the 50 hPa drop temperatures (based on the second
311 derivative minima of total HNO$_3$ averaged in 1°×1° grid cells) inside a region delimited by a PV value
312 of -8×10^{-5} K.m^2.kg^{-1}.s^{-1}, for each year of the IASI period. The green contour represents the PV isocontour
313 of -10×10^{-5} K.m^2.kg^{-1}.s^{-1}, averaged over the period 10 May – 15 July for each year, which delimits our
314 region of interest. The isocontours of 195 K for the average temperatures and the minimum temperatures,
315 as well as the isocontour of -10×10^{-5} K.m^2.kg^{-1}.s^{-1} for the minimum PV encountered at 50 hPa over the
316 10 May to 15 July period are also represented. The calculated drop temperatures corresponding to the
317 onset of HNO$_3$ depletion inside the averaged PV isocontour are found to vary between ~180 and ~210
318 K and the corresponding dates range between ~mid-May and mid-July (not shown here). Note that the
319 high extremes in the drop temperature, which are found in some cases above eastern Antarctica, should
320 be considered with caution: they correspond to specific regions above ice surface with emissivity
321 features that are known to yield errors in the IASI retrievals (Hurtmans et al., 2012; Ronsmans et al.,
322 2016). Indeed, bright land surface such as ice might in some cases lead to poor HNO$_3$ retrievals.
323 Although wavenumber-dependent surface emissivity atlases are used in FORLI (Hurtmans et al., 2012),
324 this parameter remains critical and causes poorer retrievals that, in some instances, pass through the
325 series of quality filters and could affect the drop temperature calculation.
326
327 The averaged isocontour of 195 K encircles well the area of HNO$_3$ drop temperatures lower than 195 K
328 (typically from ~187 K to ~195 K), which means that the bins inside that area characterize airmasses
329 that experience the NAT threshold temperature during a long time over the 10 May – 15 July period.
330 That area encompasses the inner vortex core (delimited by the isocontour of -10×10^{-5} K.m^2.kg^{-1}.s^{-1} for
331 the PV averaged over the 10 May – 15 July period) and show pronounced minima (lower than -0.5×10^{14}
332 molec.cm^{-2}.d^{-2}) in the second derivative of the HNO$_3$ total column with respect to time (not shown here),
333 which indicate a strong and rapid HNO$_3$ depletion. The area enclosed between the two isocontours of
334 195 K for the temperatures, the averaged one and the one for the minimum temperatures, show generally
335 higher drop temperatures and weakest minima (larger than -0.5×10^{14} molec.cm^{-2}.d^{-2}) in the second
336 derivative of the HNO$_3$ total column (not shown). That area is also enclosed by the isocontour of -10×10^{-5}
337 ^{5} K.m^2.kg^{-1}.s^{-1} for the minimum PV, meaning that the bins inside correspond, at least for one day over
338 the 10 May – 15 July period, to airmasses located at the inner edge of the vortex and characterized by
339 temperature lower than the NAT threshold temperature. The weakest minima in the second derivative
340 of total HNO$_3$ (not shown) observed in that area indicate a weak and slow HNO$_3$ depletion and might be
341 explained by a short period of the NAT threshold temperature experienced at the inner edge of the vortex.

342 It could also reflect a mixing with strong HNO_3-depleted and colder airmasses from the inner vortex
343 core. The mixing with these already depleted airmasses could also explained the higher drop
344 temperatures detected in those bins. These high drop temperatures are generally detected later (after the
345 HNO_3 depletion occurs, i.e. after the 10 May – 15 July period considered here – not shown), which
346 supports the transport, in those bins, of earlier HNO_3-depleted airmasses and the likely mixing at the
347 edge of the vortex. Finally, these spatial variations might also partly reflect the range of maximum
348 sensitivity of IASI to HNO_3, while biases in ECMWF reanalysis are too small for explaining the spatial
349 variation in drop temperatures. Thanks to the assimilation of an advanced Tiros Operational Vertical
350 Sounder (ATOVS) around 1998–2000 in reanalyses, to the better coverage of satellite instruments and
351 to the use of global navigation satellite system (GNSS) radio occultation (RO) (Schreiner et al., 2007;
352 Wang et al., 2007; Lambert and Santee, 2018; Lawrence et al., 2018), the uncertainties have been vastly
353 reduced. Comparisons of the ECMWF ERA Interim dataset used in this work with the COSMIC data
354 (Lambert and Santee, 2018) found a small warm bias, with median differences around 0.5 K, reaching
355 0–0.25 K in the southernmost regions of the globe at ~68–21 hPa where PSCs form.

357 Except above some parts of Antarctica which are prone to larger retrieval errors, the overall range in the
358 drop 50 hPa temperature for total HNO_3 inside the isocontour for the averaged temperature of 195 K,
359 typically extends from ~187 K to ~195 K, which falls within the range of PSCs nucleation temperature
360 at 50 hPa: from slightly below T_{NAT} to around 3-4 K below the ice frost point - T_{ice} - depending on
361 atmospheric conditions, on TTE and on the type of formation mechanisms (Pitts et al., 2011; Peter and
362 Grooß, 2012; Hoyle et al., 2013). This underlines well the benefit of the excellent spatial and temporal
363 coverage of IASI that allows capturing the rapid and critical depletion phase over a large scale.

365 **5 Conclusions**

367 In this paper, we have explored the added value of the dense HNO_3 total columns dataset provided by
368 the IASI/Metop satellite over a full decade (2008–2017) for monitoring the stratospheric depletion phase
369 that occurs each year in the S.H. and for investigating its relationship to the NAT formation temperature.
370 To that end, we focused on and delimited the coldest polar region of the S.H. using a specific PV value
371 at 530 K (~50 hPa, PV of -10×10^{-5} $K.m^2.kg^{-1}.s^{-1}$) and stratospheric temperatures at 50 hPa, taken from
372 the ECMWF ERA Interim reanalysis. That single representative pressure level has been considered in
373 this study given the maximum sensitivity of IASI to HNO_3 around that level over a range where the
374 PSCs formation/denitrification process occur.

376 The annual cycle of total HNO_3, as observed from IASI, has first been characterized according to the
377 temperature evolution. Three various regimes (R1 to R3) in the total HNO_3 - 50 hPa temperature
378 relationship were highlighted from the time series over the S.H. polar region and described along the
379 cycle: R1 is defined at play during April and May and characterized by a rapid decrease in 50 hPa
380 temperatures while HNO_3 accumulates in the poles; R2, from June to September, shows the onset of the
381 depletion when the 50 hPa temperatures fall below 195 K (considered here as the onset of PSCs
382 nucleation phase at that level), with a strong consistency between each year; R3, defined from November
383 until March when total HNO_3 remains at low R2 plateau levels, despite the return of sunlight and heat,
384 characterizes the strong denitrification of the stratosphere, likely due to PSCs sedimentation at lower
385 levels where the IASI sensitivity is low. For each year over the IASI period, the use of the second
386 derivative of the HNO_3 column versus time was then found particularly valuable to detect the onset of
387 the HNO_3 condensation to PSCs. It is captured, on average from IASI, a few days before June with a
388 delay of 4–23 days after the maximum in total HNO_3. Except for the year 2014, the corresponding
389 temperatures ('drop temperatures') were detected between 189.2 K and 198.6 K (194.1 ± 2.8 on average
390 over the 10 years, excluding the year 2014 that shows a drop temperature of 202.8 K), The corresponding

391 ~~temperatures ('drop temperatures') were detected between 189.2 K and 202.8 K (194.2 ± 3.8 on average~~
392 ~~over the 10 years),~~ which tends to demonstrated the good consistency between the 50 hPa drop
393 temperature and the PSCs formation temperatures in that altitude region. Finally, the annual and spatial
394 variability (within $1° \times 1°$) in the drop temperature was further explored from IASI total HNO_3. Inside
395 the isocontours of 195 K for the average temperatures and of -10×10^{-5} $K.m^2.kg^{-1}.s^{-1}$ for the averaged PV
396 at 50 hPa, the drop temperatures are detected between ~mid-May and mid-July, typically range between
397 ~187 K to ~195 K and are associated with the highest minima (lower than -0.5×10^{14} $molec.cm^{-2}.d^{-2}$) in
398 the second derivative of the HNO_3 total column with respect to time, indicating a strong and rapid HNO_3
399 depletion. Except for extreme drop temperatures (~210 K) that were found from year to year above
400 eastern Antarctica and suspected to result from unfiltered poor quality retrievals in case of emissivity
401 issues above ice, the range of drop temperatures is interestingly found in line with the PSCs nucleation
402 temperature that is known, from previous studies, to strongly depend on a series a factors (e.g.
403 meteorological conditions, HNO_3 vapour pressure, temperature threshold exposure, presence of
404 meteoritic dust). At the edge of the vortex, considering the isocontours of 195 K for the minimum
405 temperatures or of -10×10^{-5} $K.m^2.kg^{-1}.s^{-1}$ for the minimum PV, higher and later drop temperatures along
406 with weakest minima in the second derivative of the HNO_3 total column with respect to time, indicating
407 a slow HNO_3 depletion, are found. It likely results from a short temperature threshold exposure or a
408 mixing with already depleted airmasses from the inner vortex core. The results of this study highlight
409 the ability of IASI to measure the variations in total HNO_3 and, in particular, to capture and monitor the
410 rapid depletion phase over the whole polar regions.

412 We show in this study that the IASI dataset allows capturing the variability of stratospheric HNO_3
413 throughout the year (including the polar night) in the Antarctic. In that respect, it offers a new
414 observational means to monitor the relation of HNO_3 to temperature and the related formation of PSCs.
415 Despite the limited vertical resolution of IASI which does not allow to investigate the HNO_3 uptake by
416 the different types of PSCs during their formation and growth along the vertical profile, the HNO_3 total
417 column measurements from IASI constitute an important new dataset for exploring the strong polar
418 depletion over the whole stratosphere. This is particularly relevant considering the mission continuity,
419 which will span several decades with the planned follow-on missions. Indeed, thanks to the three
420 successive instruments (IASI-A launched in 2006 and still operating, IASI-B in 2012, and IASI-C in
421 2018) that demonstrate an excellent stability of the Level-1 radiances, the measurements will soon
422 provide an unprecedented long-term dataset of HNO_3 total columns. Further work could also make use
423 of this unique data set to investigate the relation between HNO_3, O_3, and meteorology in the changing
424 climate.

Data availability
The IASI HNO_3 data processed with FORLI-HNO_3 v0151001 are available upon request to the
corresponding author.

Author contributions
G.R. performed the analysis, wrote the manuscript and prepared the figures. C.W. and L.C. contributed
to the analysis. C.W., S.S., P.-F. C. and L.C. contributed to the interpretation of the results. D.H. was
responsible for the retrieval algorithm development and the processing of the IASI HNO_3 dataset. All
authors contributed to the writing of the text and reviewed the manuscript.

Competing interests
The authors declare no competing interests.

Acknowledgements

440 IASI has been developed and built under the responsibility of the Centre National d'Etudes Spatiales
441 (CNES, France). It is flown on board the Metop satellites as part of the EUMETSAT Polar System. The
442 IASI L1 data are received through the EUMETCast near-real-time data distribution service. The research
443 was funded by the F.R.S.-FNRS, the Belgian State Federal Office for Scientific, Technical and Cultural
444 Affairs (Prodex arrangement 4000111403 IASI.FLOW) and EUMETSAT through the Satellite
445 Application Facility on Atmospheric Composition Monitoring (ACSAF). G. Ronsmans is grateful to the
446 Fonds pour la Formation à la Recherche dans l'Industrie et dans l'Agriculture of Belgium for a PhD
447 grant (Boursier FRIA). L. Clarisse is a research associate supported by the F.R.S.-FNRS. C. Clerbaux is
448 grateful to CNES for financial support. S. Solomon is supported by the National Science Foundation
449 (NSF-1539972).

450
451
452
453
454
455
456
457
458
459
460
461
462
463
464
465
466
467
468
469
470
471
472
473
474
475
476
477
478
479
480
481
482
483
484
485
486
487
488

Figure captions
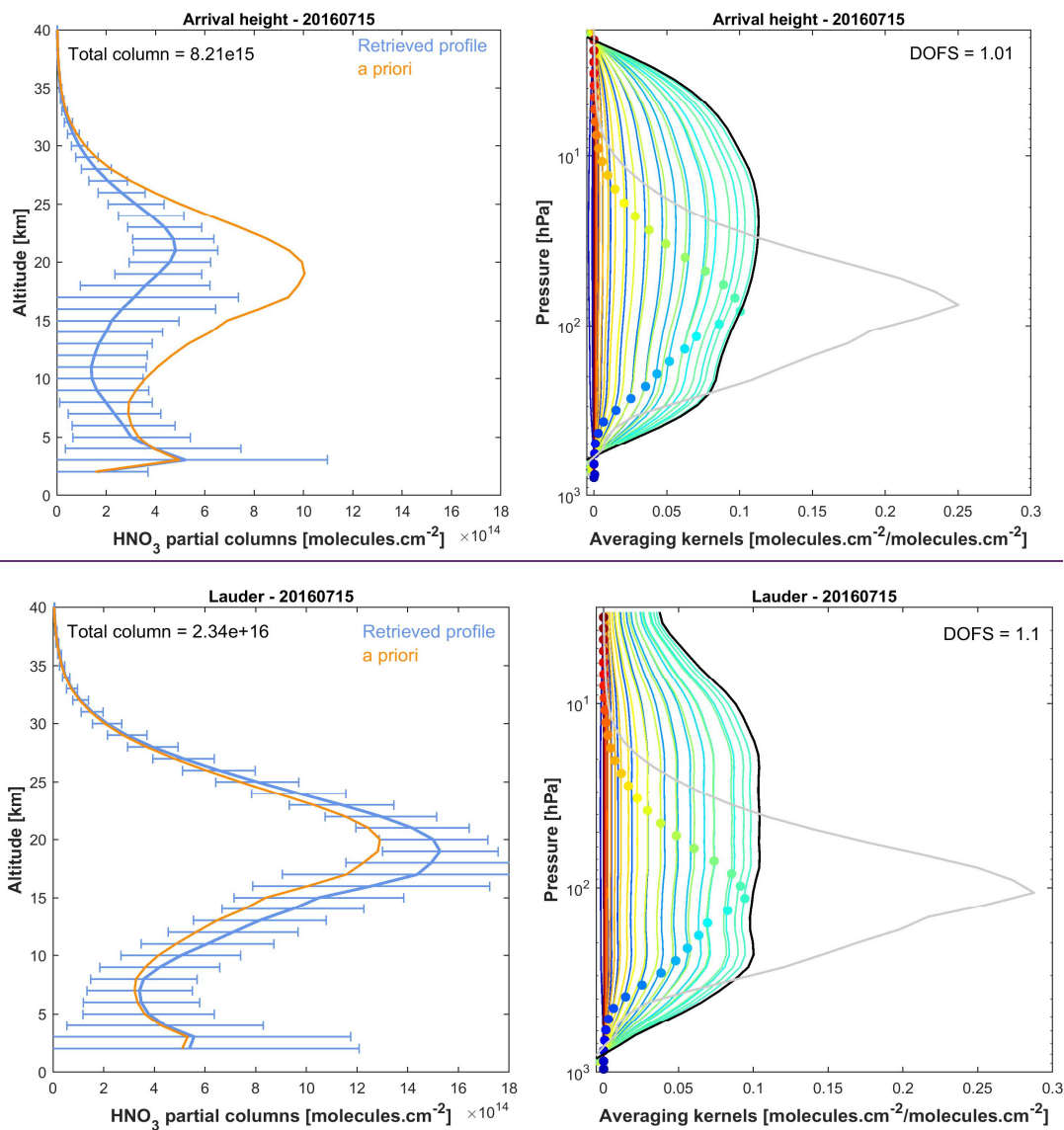
Figure 1. Examples of IASI HNO$_3$ vertical profiles (in molec.cm^{-2}) with corresponding averaging kernels (in molec.cm-^{2}/molec.cm-^{2}; with the total column averaging kernels (black) and the sensitivity profiles (grey) (divided by 10) above Arrival Height (77.49°S, 166.39°E, top panels) and Lauder (45.03°S, 169,40°E; bottom panels). The error bars associated with the HNO$_3$ vertical profile represent the total retrieval error. The a priori profile is also represented. The total column and the DOFS values are indicated.
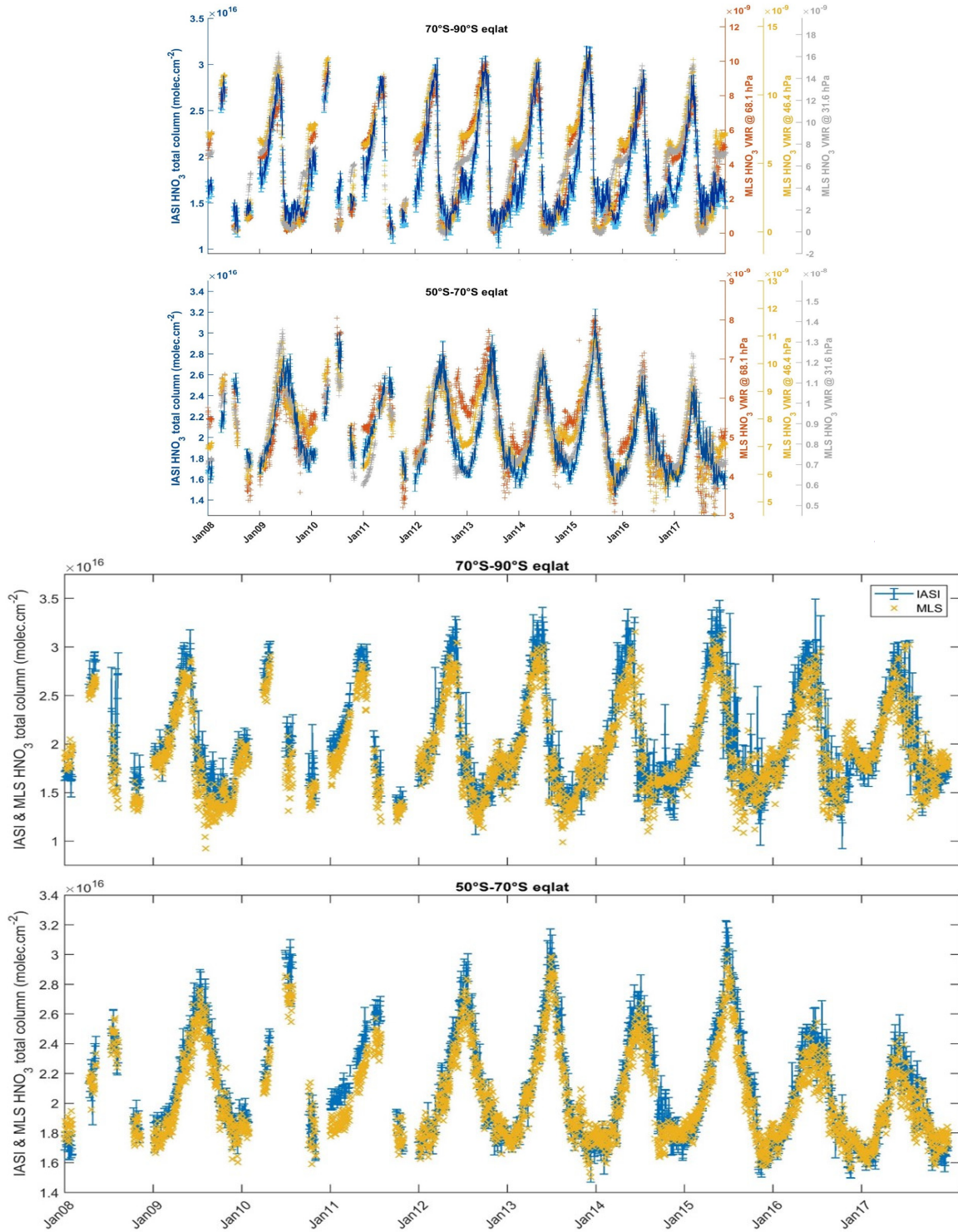
Figure ~~12~~. Time series of daily IASI total HNO$_3$ column (blue) co-located with MLS and of MLS total HNO$_3$ columns (orange) within 2.5x2.5 grid boxes, averaged in the 70°S–90°S (top panel), the 50°S–70°S (middle panel) and the 30°S–50°S (bottom panel) equivalent latitude bands. ~~Time series of daily IASI total HNO$_3$ column (blue, left y-axis) co-located with MLS and of MLS VMR HNO$_3$ within 2.5×2.5 grid boxes at three pressure levels (at 30, 50 and 70 hPa; right y-axis), averaged in the 70°S–90°S (top panel) and in the 50°S–70°S (bottom panel) equivalent latitude bands.~~ The error bars (~~light~~ blue) represents 3σ, where σ is the standard deviation around the IASI HNO$_3$ daily average.

510
511
512
513
514
515
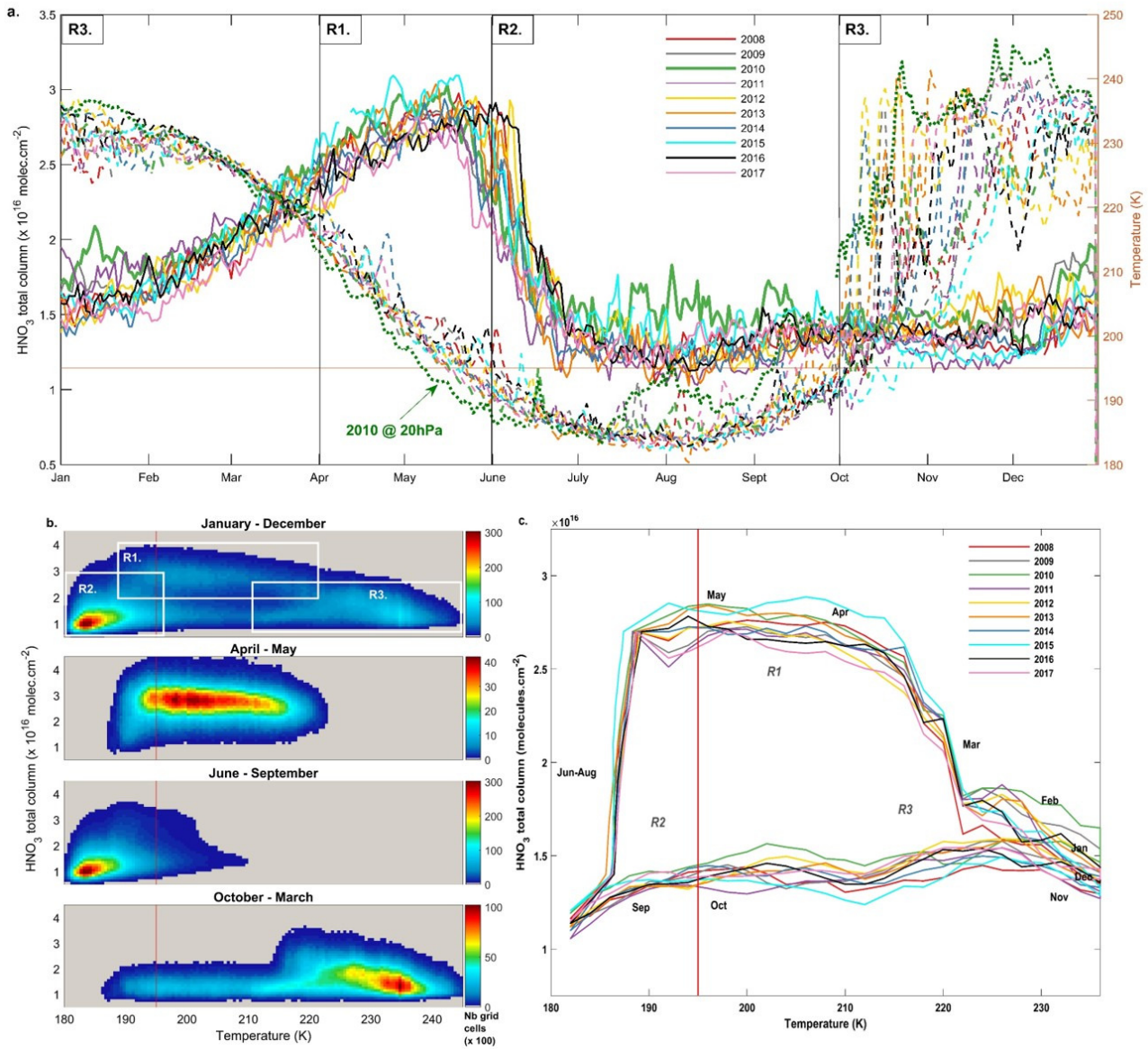
516
517
518 **Figure 23.** (a) Time series of daily averaged HNO₃ total columns (solid lines) and temperatures taken at 50 hPa
519 (dashed lines) in the 70° - 90° S equivalent latitude band, for the years 2008 – 2017. The green dotted line
520 represents the temperatures at 20 hPa for the year 2010. (b) HNO₃ total columns versus temperatures (at 50 hPa)
521 histogram for the whole year (top) and for the 3 defined regimes (R1 - R3) separated in (a) for the year 2011. The
522 colors refer to the number of gridded measurements in each cell. (c) Evolution of daily averaged HNO₃ total
523 columns with the highest occurrence (in bins of 0.1×10^{16} molec.cm⁻² and 2 K) as a function of the 50 hPa
524 temperature for the years 2008 – 2017. The red horizontal or vertical lines represent the 195 K threshold
525 temperature.
526

527
528
529
530
531
532
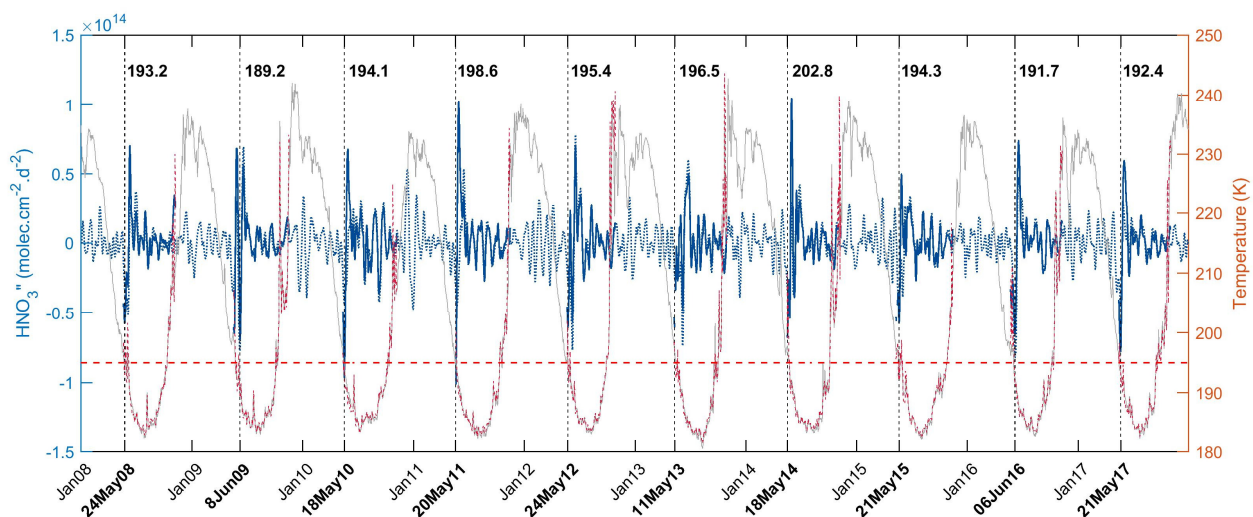
533
534
535 **Figure 34.** Time series of total HNO_3 second derivative (blue, left y-axis) and of the temperature (red, right y-
536 axis), in the region of potential vorticity at 530 K lower than -10×10^{-5} $K.m^2.kg^{-1}.s^{-1}$. The red horizontal line
537 corresponds to the 195 K temperature. The vertical dashed lines indicate the second derivative minimum in HNO_3
538 for each year. The corresponding dates (in bold, on the x-axis) and temperatures are also indicated. The time series
539 of total HNO_3 second derivative (dashed blue) and of temperature (grey) in the 70° – 90° S Eqlat band are also
540 represented.

541
542
543
544
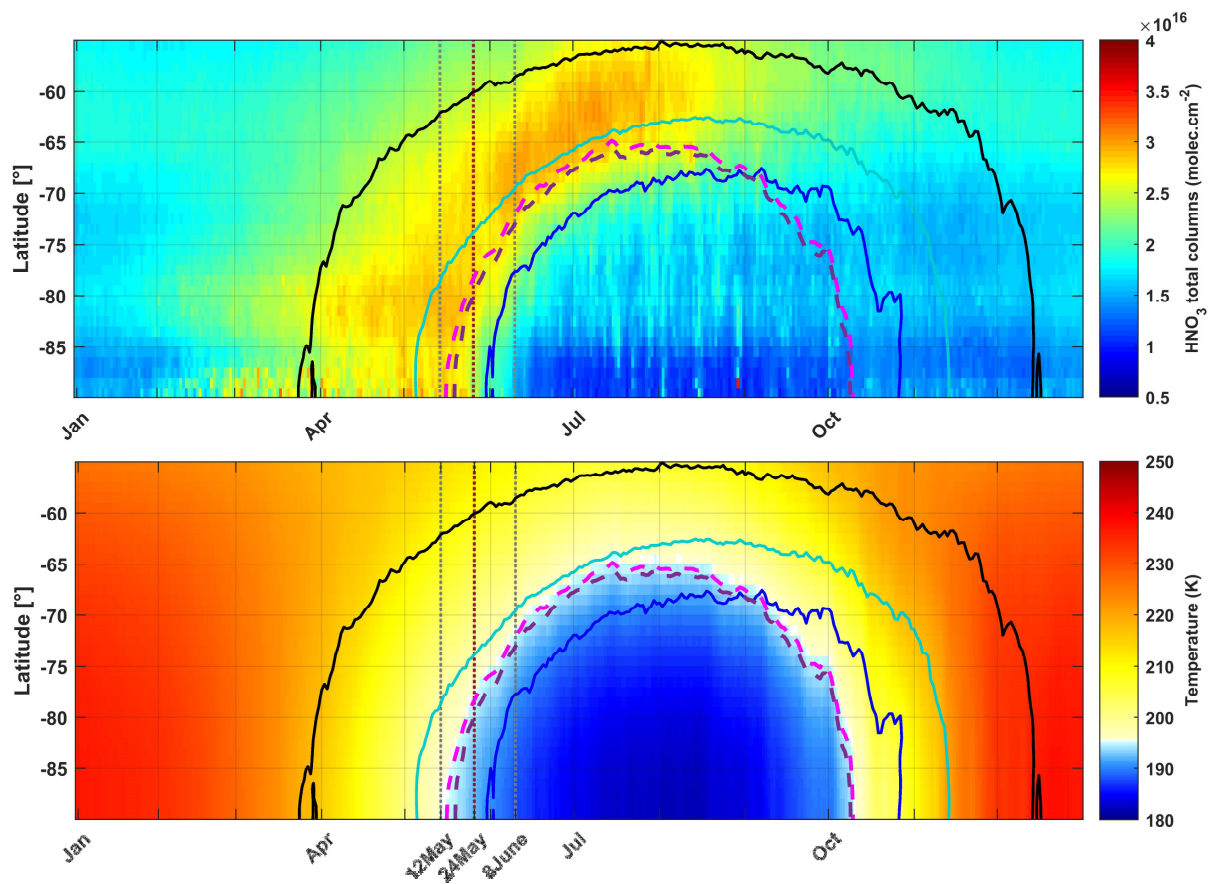
Figure 45. Zonal distributions of (a) HNO₃ total columns (in molec.cm⁻²) from IASI and (b) temperatures at 50 hPa from ERA Interim (in K) between 55° to 90° south and averaged over the years 2008 – 2017. Three isocontours for PV of -5 (black), -8 (cyan) and -10 (blue) (×10⁻⁵ K.m².kg⁻¹.s⁻¹) at 530 K, the isocontours for the 195 K temperature (pink) and for the averaged 194.2 K drop temperature (purple) at 50 hPa are superimposed. The vertical grey dashed lines encompass the period of the second derivative minima and the red one indicates the average date for the drop temperatures calculated in the area delimited by a -10×10⁻⁵ K.m².kg⁻¹.s⁻¹ PV contour.
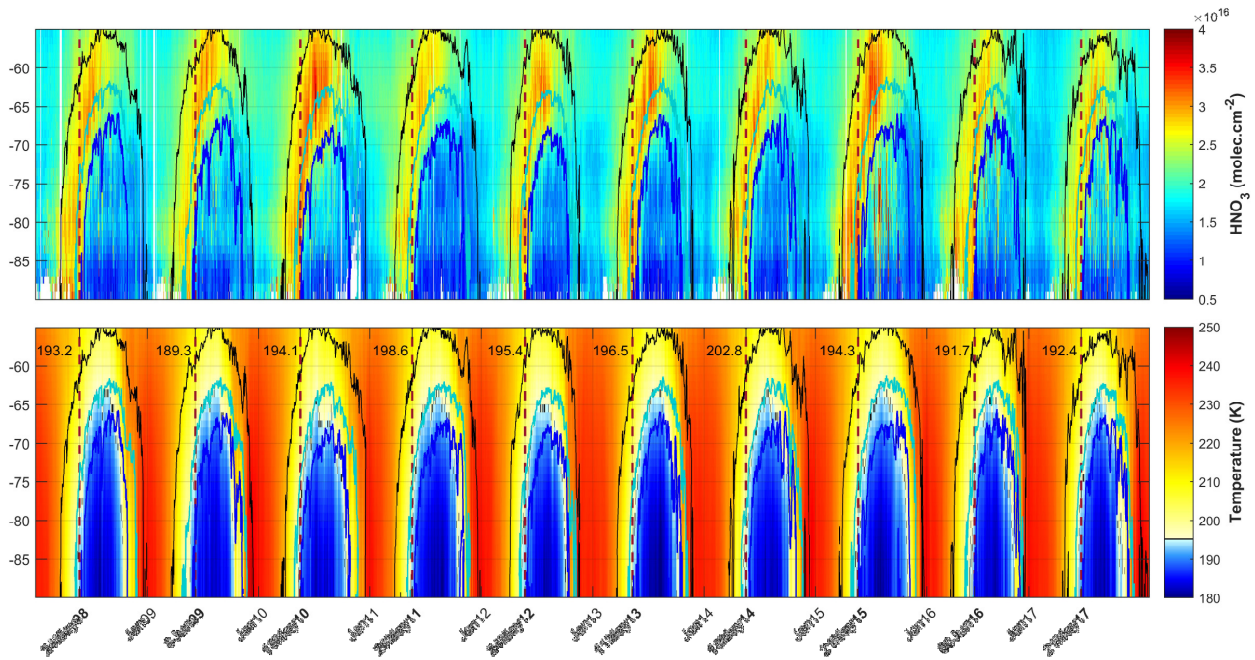
553
554 **Figure 56.** Zonally averaged distributions of (top) HNO₃ total columns (in molec.cm⁻²) from IASI and (bottom)
555 temperatures at 50 hPa from ERA Interim (in K). The latitude range is from 55° to 90° south and the isocontours
556 are PVs of -5 (black), -8 (cyan) and -10 (blue) (× 10⁻⁵ K.m².kg⁻¹.s⁻¹ at 530 K). The vertical red dashed lines
557 correspond to the second derivative minima each year in the area delimited by a -10×10⁻⁵ K.m².kg⁻¹.s⁻¹ PV contour.
558
559

Figure 6_7_. Spatial distribution (1°×1°) of the drop temperature at 50 hPa (K) (calculated from the total HNO$_3$ second derivative minima) for each year of IASI (2008–2017), in a region defined by a PV of -8×10^{-5} K.m^2.kg^{-1}.s^{-1}. The isocontours of -10×10^{-5} K.m^2.kg^{-1}.s^{-1} at 530 K for the averaged PV (in green) and the minimum PV (in cyan) encountered over the period 10 May –15 June for each year and the isocontours of 195 K at 50 hPa for the averaged (in red) and the minimum (in pink) temperatures over the same period are represented.

560
561
562
563
564
565
566
567
568
569
570
571
572
573
574
575
576
577
578
579
580

References

Braun, M., Grooß, J.-U., Woiwode, W., Johansson, S., Höpfner, M., Friedl-Vallon, F., Oelhaf, H., Preusse, P., Ungermann, J., Sinnhuber, B.-M., Ziereis, H., and Braesicke, P.: Nitrification of the lowermost stratosphere during the exceptionally cold Arctic winter 2015/16, Atmospheric Chemistry and Physics Discussions, https://doi.org/10.5194/acp-2019-108, 2019.

Carslaw, K. S., Luo, B. P., and Peter, T.: An analytical expression for the composition of aqueous {HNO$_3$-H$_2$SO$_4$-H$_2$O} stratospheric aerosols including gas phase removal of HNO$_3$, Geophys. Res. Lett., 22, 1877–1880, https://doi.org/10.1029/95GL01668, 1995.

Carslaw, K. S., Wirth, M., Tsias, A., Luo, B. P., Dörnbrack, A., Leutbecher, M., Volkert, H., Renger, W., Bacmeister, J. T., Reimer, E., and Peter, T.: Increased stratospheric ozone depletion due to mountain-induced atmospheric waves, Nature, 391, 675–678, https://doi.org/10.1038/35589, 1998.

Clerbaux, C., Boynard, A., Clarisse, L., George, M., Hadji-Lazaro, J., Herbin, H., Hurtmans, D., Pommier, M., Razavi, A., Turquety, S., Wespes, C., and Coheur, P.-F.: Monitoring of atmospheric composition using the thermal infrared IASI/MetOp sounder, Atmospheric Chemistry and Physics, 9, 6041–6054, https://doi.org/10.5194/acp-9-6041-2009, 2009.

de Laat, A. T. J. and van Weele, M.: The 2010 Antarctic ozone hole: Observed reduction in ozone destruction by minor sudden stratospheric warmings, Scientific Reports, 1, 38, https://doi.org/10.1038/srep00038, 2011.

de Zafra, R. and Smyshlyaev, S. P.: On the formation of HNO3 in the Antarctic mid to upper stratosphere in winter, Journal of Geophysical Research, 106, 23 115, https://doi.org/10.1029/2000JD000314, 2001.

Grooß, J. U., Engel, I., Borrmann, S., Frey, W., Günther, G., Hoyle, C. R., Kivi, R., Luo, B. P., Molleker, S., Peter, T., Pitts, M. C., Schlager, H., Stiller, G., Vömel, H., Walker, K. a., and Müller, R.: Nitric acid trihydrate nucleation and denitrification in the Arctic stratosphere, Atmospheric Chemistry and Physics, 14, 1055–1073, https://doi.org/10.5194/acp-14-1055-2014, 2014.

Hanson, D. and Mauersberger, K.: Laboratory studies of the nitric acid trihydrate: Implications for the south polar stratosphere, Geophysical Research Letters, 15, 855–858, https://doi.org/10.1029/GL015i008p00855, 1988.

Harris, N. R. P., Lehmann, R., Rex, M., and von der Gathen, P.: A closer look at Arctic ozone loss and polar stratospheric clouds, Atmospheric Chemistry and Physics, 10, 8499–8510, https://doi.org/10.5194/acp-10-8499-2010, 2010.

Hilton, F., Armante, R., August, T., Barnet, C., Bouchard, A., Camy-Peyret, C., Capelle, V., Clarisse, L., Clerbaux, C., Coheur, P.-F., Collard, A., Crevoisier, C., Dufour, G., Edwards, D., Faijan, F., Fourrié, N., Gambacorta, A., Goldberg, M., Guidard, V., Hurtmans, D., Illingworth, S., Jacquinet-Husson, N., Kerzenmacher, T., Klaes, D., Lavanant, L., Masiello, G., Matricardi, M., McNally, A., Newman, S., Pavelin, E., Payan, S., Péquignot, E., Peyridieu, S., Phulpin, T., Remedios, J., Schlüssel, P., Serio, C., Strow, L., Stubenrauch, C., Taylor, J., Tobin, D., Wolf, W., and Zhou, D.: Hyperspectral Earth Observation from IASI: Five Years of Accomplishments, Bulletin of the American Meteorological Society, 93, 347–370, https://doi.org/10.1175/BAMS-D-11-00027.1, 2012.

Hoffmann, L., Spang, R., Orr, A., Alexander, M. J., Holt, L. A., and Stein, O.: A decadal satellite record of gravity wave activity in the lower stratosphere to study polar stratospheric cloud formation, Atmospheric Chemistry and Physics, 17, 2901–2920, https://doi.org/10.5194/acp-17-2901-2017, 2017.

Höpfner, M., Luo, B. P., Massoli, P., Cairo, F., Spang, R., Snels, M., Di Donfrancesco, G., Stiller, G., von Clarmann, T., Fischer, H., and Biermann, U.: Spectroscopic evidence for NAT, STS, and ice in MIPAS infrared limb emission measurements of polar stratospheric clouds, Atmospheric Chemistry and Physics, 6, 1201–1219, https://doi.org/10.5194/acp-6-1201-2006, 2006.

Höpfner, M., Pitts, M. C., and Poole, L. R.: Comparison between CALIPSO and MIPAS observations of polar stratospheric clouds, Journal of Geophysical Research Atmospheres, 114, 1–15, https://doi.org/10.1029/2009JDO12114, 2009.

Hoyle, C. R., Engel, I., Luo, B. P., Pitts, M. C., Poole, L. R., Grooß, J. U., and Peter, T.: Heterogeneous formation of polar stratospheric clouds- Part 1: Nucleation of nitric acid trihydrate (NAT), Atmospheric Chemistry and Physics, 13, 9577–9595, https://doi.org/10.5194/acp-13- 9577-2013, 2013.

Hurtmans, D., Coheur, P.-F., Wespes, C., Clarisse, L., Scharf, O., Clerbaux, C., Hadji-Lazaro, J., George, M., and Turquety, S.: FORLI radiative transfer and retrieval code for IASI, Journal of Quantitative Spectroscopy and Radiative Transfer, 113, 1391–1408, https://doi.org/10.1016/j.jqsrt.2012.02.036, 2012.

James, A. D., Brooke, J. S. A., Mangan, T. P., Whale, T. F., Plane, J. M. C., and Murray, B. J.: Nucleation of nitric acid hydrates in polar stratospheric clouds by meteoric material, Atmospheric Chemistry and Physics, 18, 4519–4531, https://doi.org/10.5194/acp-18-4519- 2018, 2018.

Keys, J. G., Johnston, P. V., Blatherwick, R. D., and Murcray, F. J.: Evidence for heterogeneous reactions in the Antarctic autumn stratosphere, Nature, 361, 49–51, https://doi.org/10.1038/361049a0, 1993.

Klekociuk, A., Tully, M., Alexander, S., Dargaville, R., Deschamps, L., Fraser, P., Gies, H., Henderson, S., Javorniczky, J., Krummel, P., Petelina, S., Shanklin, J., Siddaway, J., and Stone, K.: The Antarctic ozone hole during 2010, Australian Meteorological and Oceanographic Journal, 61, 253–267, https://doi.org/10.22499/2.6104.006, 2011.

Koop, T., Luo, B., Tsias, A., and Peter, T.: Water activity as the determinant for homogeneous ice nucleation in aqueous solutions, Nature, 406, 611–614, https://doi.org/10.1038/35020537, 2000.

Kvissel, O.-K., Orsolini, Y. J., Stordal, F., Isaksen, I. S. A., and Santee, M. L.: Formation of stratospheric nitric acid by a hydrated ion cluster reaction: Implications for the effect of energetic particle precipitation on the middle atmosphere, Journal of Geophysical Research: Atmospheres, 117, n/a–n/a, https://doi.org/10.1029/2011jd017257, 2012.

Lambert, A. and Santee, M. L.: Accuracy and precision of polar lower stratospheric temperatures from reanalyses evaluated from A-Train CALIOP andMLS, COSMIC GPS RO, and the equilibrium thermodynamics of supercooled ternary solutions and ice clouds, Atmospheric Chemistry and Physics, 18, 1945–1975, https://doi.org/10.5194/acp-18-1945-2018, 2018.

Lambert, A., Santee, M. L., Wu, D. L., and Chae, J. H.: A-train CALIOP and MLS observations of early winter Antarctic polar stratospheric clouds and nitric acid in 2008, Atmospheric Chemistry and Physics, 12, 2899–2931, https://doi.org/10.5194/acp-12-2899-2012, 2012.

Lambert, A., Santee, M. L., and Livesey, N. J.: Interannual variations of early winter Antarctic polar stratospheric cloud formation and nitric acid observed by CALIOP and MLS, Atmospheric Chemistry and Physics, 16, 15 219–15 246, https://doi.org/10.5194/acp-16-15219-2016, 2016.

Lawrence, Z. D., Manney, G. L., and Wargan, K.: Reanalysis intercomparisons of stratospheric polar processing diagnostics, Atmospheric Chemistry and Physics, 18, 13 547–13 579, https://doi.org/10.5194/acp-18-13547-2018, 2018.

Lowe, D. and MacKenzie, A. R.: Polar stratospheric cloud microphysics and chemistry, Journal of Atmospheric and Solar-Terrestrial Physics, 70, 13–40, https://doi.org/10.1016/j.jastp.2007.09.011, 2008.

Molleker, S., Borrmann, S., Schlager, H., Luo, B., Frey, W., Klingebiel, M., Weigel, R., Ebert, M., Mitev, V., Matthey, R., Woiwode, W., Oelhaf, H., Dörnbrack, A., Stratmann, G., Grooß, J.-U., Günther, G., Vogel, B., Müller, R., Krämer, M., Meyer, J., and Cairo, F.: Microphysical properties of synoptic-scale polar stratospheric clouds: in situ measurements of unexpectedly large HNO_3-containing particles in the Arctic vortex, Atmospheric Chemistry and Physics, 14, 10 785–10 801, https://doi.org/10.5194/acp-14-10785-2014, 2014.

Murphy, D. M. and Koop, T.: Review of the vapour pressures of ice and supercooled water for atmospheric applications, Quarterly Journal of the Royal Meteorological Society, 131, 1539–1565, https://doi.org/10.1256/qj.04.94, 2005.

Peter, T.: Microphysics and heterogeneous chemistry of polar stratospheric clouds, Annual Review of Physical Chemistry, 48, 785–822, https://doi.org/10.1146/annurev.physchem.48.1.785, 1997.

Peter, T. and Grooß, J.-U.: Chapter 4. Polar Stratospheric Clouds and Sulfate Aerosol Particles: Microphysics, Denitrification and Heterogeneous Chemistry, in: Stratospheric Ozone Depletion and Climate Change, pp. 108–144, Royal Society of Chemistry, https://doi.org/10.1039/9781849733182-00108, 2012.

Piccolo, C. and Dudhia, A.: Precision validation of MIPAS-Envisat products, Atmospheric Chemistry and Physics, 7, 1915–1923, https://doi.org/10.5194/acp-7-1915-2007, 2007.

Pitts, M. C., Poole, L. R., Dörnbrack, A., and Thomason, L. W.: The 2009-2010 Arctic polar stratospheric cloud season: A CALIPSO perspective, Atmospheric Chemistry and Physics, 11, 2161–2177, https://doi.org/10.5194/acp-11-2161-2011, 2011.

Pitts, M. C., Poole, L. R., Lambert, A., and Thomason, L.W.: An assessment of CALIOP polar stratospheric cloud composition classification, Atmospheric Chemistry and Physics, 13, 2975–2988, https://doi.org/10.5194/acp-13-2975-2013, 2013.

Pitts, M. C., Poole, L. R., and Gonzalez, R.: Polar stratospheric cloud climatology based on CALIPSO spaceborne lidar measurements from 2006 to 2017, Atmospheric Chemistry and Physics, 18, 10 881–10 913, https://doi.org/10.5194/acp-18-10881-2018, 2018.

Rodgers, C. D.: Inverse Methods for Atmospheric Sounding - Theory and Practice, vol. 2 of Series on Atmospheric Oceanic and Planetary Physics, World Scientific Publishing Co. Pte. Ltd., https://doi.org/10.1142/9789812813718, 2000.

Ronsmans, G., Langerock, B., Wespes, C., Hannigan, J. W., Hase, F., Kerzenmacher, T., Mahieu, E., Schneider, M., Smale, D., Hurtmans, D., De Mazière, M., Clerbaux, C., and Coheur, P.-F.: First characterization and validation of FORLI-HNO3 vertical profiles retrieved from IASI/Metop, Atmospheric Measurement Techniques, 9, 4783–4801, https://doi.org/10.5194/amt-9-4783-2016, 2016.

Ronsmans, G.,Wespes, C., Hurtmans, D., Clerbaux, C., and Coheur, P.-F.: Spatio-temporal variations of nitric acid total columns from 9 years of IASI measurements – a driver study, Atmospheric Chemistry and Physics, 18, 4403–4423, https://doi.org/10.5194/acp-18-4403-2018, 2018.

Santee, M. L., Manney, G. L., Froidevaux, L., Read, W. G., and Waters, J. W.: Six years of UARS Microwave Limb Sounder HNO_3 observations : Seasonal, interhemispheric, and interannual variations in the lower stratosphere, Journal of Geophysical Research, 104, 8225–8246, https://doi.org/10.1029/1998JD100089, 1999.

Santee, M. L., Lambert, A., Read, W. G., Livesey, N. J., Cofield, R. E., Cuddy, D. T., Daffer, W. H., Drouin, B. J., Froidevaux, L., Fuller, R. A., Jarnot, R. F., Knosp, B. W., Manney, G. L., Perun, V. S., Snyder, W. V., Stek, P. C., Thurstans, R. P., Wagner, P. A., Waters, J. W., Muscari, G., de Zafra, R. L., Dibb, J. E., Fahey, D. W., Popp, P. J., Marcy, T. P., Jucks, K. W., Toon, G. C., Stachnik, R. A., Bernath, P. F., Boone, C. D., Walker, K. A., Urban, J., and Murtagh, D.: Validation of the Aura Microwave Limb Sounder HNO3 measurements, Journal of Geophysical Research, 112, 1–22, https://doi.org/10.1029/2007JD008721, 2007.

Schreiner, J., Voigt, C., Weisser, C., Kohlmann, A., Mauersberger, K., Deshler, T., Kröger, C., Rosen, J., Kjome, N., Larsen, N., Adriani, A., Cairo, F., Donfrancesco, G. D., Ovarlez, J., Ovarlez, H., and Dörnbrack, A.: Chemical , microphysical , and optical properties of polar stratospheric clouds, Journal of Geophysical Research, 108, 1–10, https://doi.org/10.1029/2001JD000825, 2003.

Schreiner, W., Rocken, C., Sokolovskiy, S., Syndergaard, S., and Hunt, D.: Estimates of the precision of GPS radio occultations from the COSMIC/FORMOSAT-3 mission, Geophysical Research Letters, 34, 1–5, https://doi.org/10.1029/2006GL027557, 2007.

Sheese, P. E., Walker, K. A., Boone, C. D., Bernath, P. F., Froidevaux, L., Funke, B., Raspollini, P., and von Clarmann, T.: ACE-FTS ozone, water vapour, nitrous oxide, nitric acid, and carbon monoxide profile comparisons with MIPAS and MLS, Journal of Quantitative Spectroscopy and Radiative Transfer, 186, 63–80, https://doi.org/10.1016/j.jqsrt.2016.06.026, 2017.

Snels, M., Scoccione, A., Liberto, L. D., Colao, F., Pitts, M., Poole, L., Deshler, T., Cairo, F., Cagnazzo, C., and Fierli, F.: Comparison of Antarctic polar stratospheric cloud observations by ground-based and space-borne lidar and relevance for chemistry–climate models, Atmospheric Chemistry and Physics, 19, 955–972, https://doi.org/10.5194/acp-19-955-2019, 2019.

Solomon, S.: Stratospheric ozone depletion: A review of concepts and history, Reviews of Geophysics, 37, 275–316, https://doi.org/10.1029/1999RG900008, 1999.

Spang, R., Hoffmann, L., Höpfner, M., Griessbach, S., Müller, R., Pitts, M. C., Orr, A. M. W., and Riese, M.: A multi-wavelength classification method for polar stratospheric cloud types using infrared limb spectra, Atmospheric Measurement Techniques, 9, 3619–3639, https://doi.org/10.5194/amt-9-3619-2016, 2016.

Spang, R., Hoffmann, L., Müller, R., Grooß, J.-U., Tritscher, I., Höpfner, M., Pitts, M., Orr, A., and Riese, M.: A climatology of polar stratospheric cloud composition between 2002 and 2012 based on MIPAS/Envisat observations, Atmospheric Chemistry and Physics, 18, 5089–5113, https://doi.org/10.5194/acp-18-5089-2018, 2018.

Toon, O. B., Hamill, P., Turco, R. P., and Pinto, J.: Condensation of HNO3 and HCl in the winter polar stratospheres, Geophysical Research Letters, 13, 1284–1287, https://doi.org/10.1029/GL013i012p01284, 1986.

Urban, J., Pommier, M., Murtagh, D. P., Santee, M. L., and Orsolini, Y. J.: Nitric acid in the stratosphere based on Odin observations from 2001 to 2009 – Part 1: A global climatology, Atmospheric Chemistry and Physics, 9, 7031–7044, https://doi.org/10.5194/acp-9-7031- 2009, 2009.

Voigt, C., Schreiner, J., Kohlmann, A., Zink, P., Mauersberger, K., Larsen, N., Deshler, T., Kro, C., Rosen, J., Adriani, A., Cairo, F., Donfrancesco, G. D., Viterbini, M., Ovarlez, J., Ovarlez, H., and David, C.: Nitric Acid Trihydrate (NAT) in Polar Stratospheric Clouds, Science, 290, 1756–1758, https://doi.org/10.1126/science.290.5497.1756, 2000.

Voigt, C., Schlager, H., Luo, B. P., Dörnbrack, A., Roiger, A., Stock, P., Curtius, J., Vössing, H., Borrmann, S., Davies, S., Konopka, P., Schiller, C., Shur, G., and Peter, T.: Nitric Acid Trihydrate (NAT) formation at low NAT supersaturation in Polar Stratospheric Clouds (PSCs), Atmospheric Chemistry and Physics, 5, 1371–1380, https://doi.org/10.5194/acp-5-1371-2005, 2005.

von König, M.: Using gas-phase nitric acid as an indicator of PSC composition, Journal of Geophysical Research, 107, https://doi.org/10.1029/2001jd001041, 2002.

Wang, D. Y., Blom, C. E., Ward, W. E., Fischer, H., Blumenstock, T., Hase, F., Keim, C., Liu, G. Y., Mikuteit, S., Oelhaf, H., Wetzel, G., Cortesi, U., Mencaraglia, F., Bianchini, G., Redaelli, G., Pirre, M., Catoire, V., Huret, N., Vigouroux, C., Mahieu, E., Demoulin, P.,Wood, S., Smale, D., Jones, N., Nakajima, H., Sugita, T., Urban, J., Murtagh, D., Boone, C. D., Bernath, P. F., Walker, K. a., Kuttippurath, J.,Toon, G., Piccolo, C., Brunswick, N., Zealand, N., Science, S., and Cedex, P.: Validation of MIPAS HNO3 operational data, Atmospheric Chemistry and Physics, 7, 4905–4934, https://doi.org/10.5194/acp-7-4905-2007, 2007.

Wang, X. and Michelangeli, D. V.: A review of polar stratospheric cloud formation, China Particuology, 4, 261–271, https://doi.org/10.1016/S1672-2515(07)60275-9, 2006.

Wegner, T., Grooß, J.-U., von Hobe, M., Stroh, F., Sumin´ska-Ebersoldt, O., Volk, C. M., Hösen, E., Mitev, V., Shur, G., and Müller, R.: Heterogeneous chlorine activation on stratospheric aerosols and clouds in the Arctic polar vortex, Atmospheric Chemistry and Physics, 12, 11 095–11 106, https://doi.org/10.5194/acp-12-11095-2012, 2012.

Wespes, C., Hurtmans, D., Clerbaux, C., and Coheur, P.-F.: O₃ variability in the troposphere as observed by IASI over 2008-2016: Contribution of atmospheric chemistry and dynamics, Journal of Geophysical Research: Atmospheres, 122, 2429–2451, https://doi.org/10.1002/2016JD025875, http://doi.wiley.com/10.1002/2016JD025875, 2017.

WMO: Scientific Assessment of Ozone Depletion: 2014, Global Ozone Research and Monitoring Project – Report No. 55, World Meteorological Organization, Geneva, Switzerland, 2014.

Zhu, Y., Toon, O. B., Lambert, A., Kinnison, D. E., Brakebusch, M., Bardeen, C. G., Mills, M. J., and English, J. M.: Development of a Polar Stratospheric Cloud Model within the Community Earth System Model using constraints on Type I PSCs from the 2010-2011 Arctic winter, Journal of Advances in Modeling Earth Systems, 7, 551–585, https://doi.org/10.1002/2015ms000427, 2015.